Chemical Science

ROYAL SOCIETY OF CHEMISTRY

EDGE ARTICLE

View Article Online
View Journal | View Issue

Cite this: *Chem. Sci.*, 2020, **11**, 1299

All publication charges for this article have been paid for by the Royal Society of Chemistry

In vivo therapeutic response monitoring by a self-reporting upconverting covalent organic framework nanoplatform†

Peng Wang,‡ Fang Zhou,‡ Kesong Guan, Youjuan Wang, Xiaoyi Fu, Yue Yang, Xia Yin, Guosheng Song,* Xiao-Bing Zhang* and Weihong Tan

Received 27th September 2019
Accepted 29th November 2019

DOI: 10.1039/c9sc04875h

rsc.li/chemical-science

The real-time and *in situ* monitoring of reactive oxygen species (ROS) generation is critical for minimizing the nonspecific damage derived from the high doses of ROS required during the photodynamic therapy (PDT) process. However, phototherapeutic agents that can generate ROS-related imaging signals during PDT are rare, hampering the facile prediction of the future therapeutic outcome. Herein, we develop an upconverting covalent organic framework (COF) nanoplatform *via* a core-mediated strategy and further functionalized it with a singlet oxygen reporter for the efficient near-infrared activated and *in situ* self-reporting of PDT. In this work, the COF photodynamic efficacy is greatly improved (12.5 times that of irregular COFs) *via* tailoring the size. Furthermore, this nanoplatform is able to not only produce singlet oxygen for PDT, but it can also emit singlet oxygen-correlated luminescence, allowing the real-time and *in situ* monitoring of the therapeutic process for cancer cells or solid tumors *in vivo via* near-infrared luminescence imaging. Thus, our core-mediated synthetic and size-tailored strategy endows the upconverting COF nanoplatform with promising abilities for high-efficacy, deep-tissue, precise photodynamic treatment.

Introduction

Reactive oxygen species (ROS)-mediated therapeutic strategies provide better options for cancer treatment, such as photodynamic therapy (PDT), sonodynamic therapy, chemodynamic therapy and radiation therapy.[1,2] The exogenous ROS derived from therapeutic agents as a result of laser irradiation/ultrasound/X-rays or chemical reactions can selectively induce efficient inhibition of cancer.[3–12] However, the required high doses of ROS for efficiently killing cancer cells may impose the potential risk of damage to normal tissue and compromise the therapeutic outcomes.[13–15] Hence, the real-time and *in situ* monitoring of ROS is really critical for determining the exact therapeutic parameters, such as the time and intensity of irradiation, the administrated dose of therapeutic agent, and the endpoint of treatment, so as to maximize the therapeutic effects and minimize unwanted side effects.[13,16]

So far, several commercialized spectroscopic probes have been successfully applied for sensing ROS in solution (Table S1†).[17–23] Regrettably, all of these available probes serve only as sensors for ROS. When monitoring the treatment process, extra therapeutic agents are still needed, which may cause *ex situ* and asynchronous therapeutic feedback.[13,21] To achieve the timely feedback of results during ROS-mediated therapy and optimize the treatment protocols, there is an urgent need to design probes integrating anticancer activity with the real-time monitoring of ROS for reporting the therapeutic efficacy. Unfortunately, to the best of our knowledge, highly efficient therapeutic agents that also enable the real-time and *in situ* evaluation of ROS generation during PDT *in vivo* are rare.[24] Recently, a kind of aggregation induced emission (AIE)-based molecular probe was developed for monitoring cellular apoptosis through binding to nuclear DNA during the process of PDT.[16,25] However, the short excitation wavelength (less than 500 nm) restricted the *in vivo* application of this strategy, and the indirect sensing of ROS limited the timeliness of the therapeutic feedback.[16,25] Thus, it is still a great challenge to undertake the real-time and *in situ* monitoring of ROS during PDT *in vivo*.

Covalent organic frameworks (COFs), entirely consisting of organic building blocks, are promising tools for biosensing and nanomedicine, owing to their diversified functionalities, large surface areas and high porosities.[26–32] The building blocks of COFs can themselves be designed as active parts, increasing efficiency when functionalizing the materials.[33] However, the

Molecular Science and Biomedicine Laboratory, State Key Laboratory of Chemo/Biosensing and Chemometrics, College of Chemistry and Chemical Engineering, College of Life Sciences, Collaborative Innovation Center for Chemistry and Molecular Medicine, Hunan University, Changsha, Hunan 410082, China. E-mail: songgs@hnu.edu.cn; xbzhang@hnu.edu.cn

† Electronic supplementary information (ESI) available. See DOI: 10.1039/c9sc04875h

‡ P. Wang and F. Zhou contributed equally.

use of porphyrin based-COF systems for *in vivo* applications is still hampered by the following intrinsic limitations. (i) The optimal size of materials showing effective bioavailability is below 200 nm.[27] Unfortunately, up to now, it still remains a huge challenge to synthesize COFs with controlled nanoscale size (below 200 nm) and uniform morphology. Traditional solvothermal synthesis usually results in micron-level COFs. Although COF nanosheets can be obtained *via* the solvent-assisted exfoliation of bulk COFs,[26] the acquired COF nanosheet mixtures with various sizes and morphologies are difficult to isolate, inducing lower bioavailability and affecting the photodynamic efficacy. (ii) The photodynamic effects of COFs are stimulated by visible light (less than 700 nm), which can be attenuated by endogenous biomolecules (such as hemoglobin and melanin) and, therefore, has a low tissue penetration depth.[34–41] Until now, near-infrared (NIR) excited porphyrin based-COF systems for PDT *in vivo* have not been reported. Thus, we anticipate that the design and synthesis of size-controllable and NIR excited nanoscale COFs could open up new routes for efficient PDT *in vivo*.

To overcome these limitations, herein, we developed an upconverting COF nanoplatform for efficient NIR activated and *in situ* self-reporting PDT. Based on a lanthanide-doped upconversion nanoparticle (UCNP) core,[42–53] we realized the controlled synthesis of nanoscale COFs with various shell thicknesses *via* core-mediated imine polymerization on the UCNPs, which were termed **UCCOFs** (Scheme 1a). After tailoring the COF shell thickness, the photodynamic efficacy of the **UCCOFs** was greatly improved, becoming 12.5 times that of irregular COFs. Owing to the UCNP core demonstrating NIR excitation and anti-Stokes emission, **UCCOFs** allow efficient PDT *in vivo*. In order to monitor ROS production, indocyanine green (ICG) as a ROS indicator was loaded on **UCCOFs** (termed as **UCCOFs-1**) (Scheme 1a) for *in situ* self-reporting PDT (Scheme 1b). Under NIR light irradiation (980 nm), **UCCOFs-1** exhibited strong emission (541 nm and 654 nm) that could activate PDT. Specifically, the loaded ICG was gradually decomposed by $^1O_2$ during the PDT process and, thereby, the luminescence at 800 nm from **UCCOFs-1** was turned on for the real-time reporting of the location and dose of $^1O_2$ generation *in vivo*. As a consequence, **UCCOFs-1** demonstrated good correlation between luminescence intensity and treatment outcomes *in vivo*, and it may be employed to predict the therapeutic outcomes immediately after treatment.

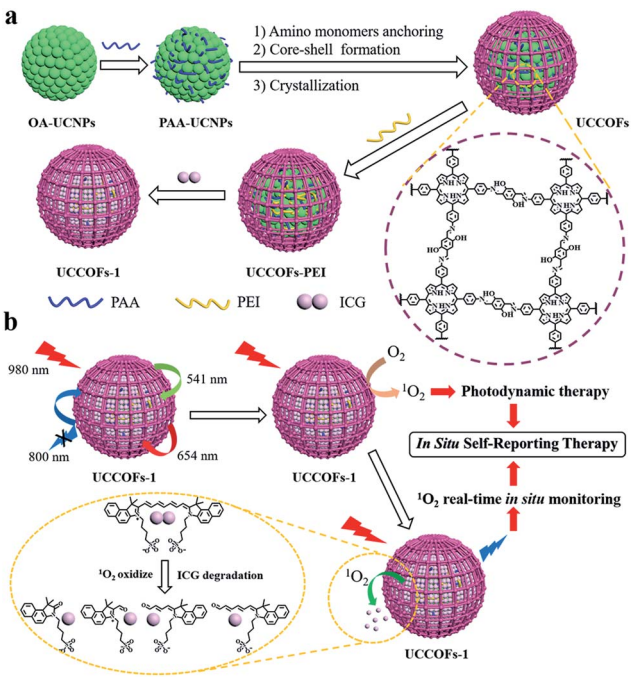

Scheme 1 (a) A schematic illustration showing the design and synthesis of the upconverting covalent organic framework nanoplatform **UCCOFs-1**. (b) A schematic illustration of the NIR-excited *in situ* self-reporting PDT process.

Results and discussion

Synthesis of UCCOFs *via* a core-mediated strategy

To obtain the desired spectroscopic properties, we firstly synthesized oleic acid-capped $NaYF_4$:20% Yb, 2% Er, 0.2% Tm UCNPs (OA-UCNPs) with a uniform size of about 30 nm, as shown in transmission electron microscopy (TEM) images (Fig. S1†). These hydrophobic nanoparticles were then surface modified with polyacrylic acid (PAA) (Fig. 1c). The PAA modification not only converted the hydrophobic OA-UCNPs into hydrophilic PAA-UCNPs, but also facilitated a core-mediated strategy for COF formation (Scheme S1†). The abundant carboxylate groups on the surface of PAA-UCNPs could provide anchors to adsorb the amino monomers of the COFs *via* H-bonding interactions. Furthermore, the carboxylate groups of PAA-UCNPs could catalyze the initial Schiff-base condensation reaction without the addition of other catalysts. With the entry of aldehyde COF monomers into the reaction system, imine polymerization only occurred on the surfaces of core particles, developing a core–shell structure. This core-mediated strategy defined the growth region of imine polymerization and contributed to the controllable synthesis of COFs. After crystallization, size-controllable nanoscale **UCCOFs** were acquired.

As proof-of-concept, porphyrin-based **UCCOFs** were prepared from the amino monomer 5,10,15,20-tetrakis(4-aminophenyl)-21*H*,23*H*-porphine (TAP) and the aldehyde monomer 2,5-dihydroxyterephthalaldehyde (DHTA) (Fig. 1b). These as-prepared **UCCOFs** exhibited a core–shell structure showing controllable size and morphology (Fig. 1d–f). The powder X-ray diffraction (PXRD) pattern showed peaks at 3.5° and 7.1° corresponding to the (100) and (200) reflection planes, consistent with COFs,[54,55] and the other peaks are assignable to UCNPs, according to JCPDS no. 28-1192 (Fig. 1g and S2†). Compared to UCNPs, the Fourier transform infrared (FTIR) spectrum of **UCCOFs** exhibited a characteristic –C=N stretching peak at 1613 cm^{-1}, suggesting imine formation on the UCNPs (Fig. 1h). The solid-state ^{13}C CP-MAS NMR spectrum of **UCCOFs** also demonstrated the core-mediated imine polymerization, showing a characteristic chemical shift at 160 ppm that originates from –C=N carbon atoms (Fig. S3†). High-resolution TEM (HRTEM) imaging showed the crystalline structure of the

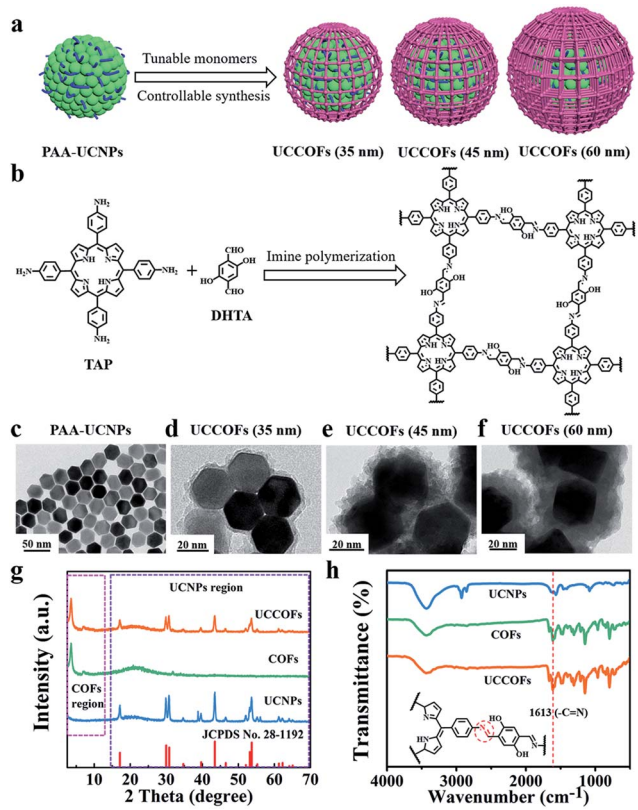

Fig. 1 The synthesis of **UCCOFs** *via* a core-mediated strategy. (a) A schematic illustration of the size-controllable synthesis of **UCCOFs**. (b) The synthesis and structures of the porphyrin-based COFs. TEM images of PAA-UCNPs (c), **UCCOFs** (35 nm) (d), **UCCOFs** (45 nm) (e) and **UCCOFs** (60 nm) (f); scale bar: 20 nm. (g) PXRD patterns of the original UCNPs, porphyrin-based COFs and **UCCOFs** compared to the standard pattern of $NaYF_4$ (JCPDS no. 28-1192). (h) FTIR spectra of the original UCNPs, porphyrin-based COFs and **UCCOFs**.

COF shells (Fig. S4†), proving that we successfully prepared **UCCOFs**.

The regulation of the building blocks endows the COFs with desired structures and diversified functionalities.[56–62] By virtue of this flexible controllability based on monomer concentrations and ratios during imine polymerization (Fig. 1a), we acquired different sizes of **UCCOFs** varying from 35 nm (Fig. 1d) to 45 nm (Fig. 1e) to 60 nm (Fig. 1f). These nanoscale **UCCOFs** were ideal for further bioapplications. We also investigated imine polymerization without template particles or with OA-UCNPs. Without the PAA-UCNP core, the COFs showed irregular sheet-like morphologies and large sizes (Fig. S5†), consistent with previous research.[55] Upon substituting OA-UCNPs for PAA-UCNPs, the sizes and morphologies of the COFs were also uncontrollable (Fig. S6†), and these are termed as irregular COFs in the discussion below.

Photochemical activity of UCCOFs

Owing to the UCNP core, **UCCOFs** have NIR excitation and anti-Stokes emission properties. The upconversion luminescence (UCL) spectrum of PAA-UCNPs exhibits characteristic emission bands at around 541 nm, 654 nm and 800 nm under 980 nm excitation (Fig. 2b). Because the UV-vis absorption of the COFs overlapped with the UCL of the UCNPs (Fig. 2b), the UCL at 541 nm and 654 nm of **UCCOFs** was quenched (Fig. 2c), indicating that effective energy transfer occurs from the UCNP core to the COF shells. Moreover, as the thickness of the COF shells increases, the UCL quenching behavior is gradually enhanced (Fig. 2c). To further demonstrate the photochemical activity, the $^1O_2$ generation by **UCCOFs** under NIR irradiation (980 nm) was evaluated using a SOSG assay (Fig. 2a). As shown in Fig. 2d, compared to free SOSG, the fluorescence intensity of SOSG at 525 nm increased as the irradiation time increased under the **UCCOF** treatment conditions, suggesting the effective photochemical activity of **UCCOFs**. The $^1O_2$ generation capacity increased as the size of **UCCOFs** increased from 35 nm to 45 nm (Fig. 2e). Notably, **UCCOFs** (45 nm) achieved more than 12-fold $^1O_2$ generation compared to irregular COFs with equivalent amounts of UCNPs and COFs (Fig. 2e). This could be ascribed to the stabilized and efficient resonance energy transfer from the UCNPs to the COFs inside **UCCOFs**, compared to the irregular COFs with their arbitrary assembly patterns. In other words, our core-mediated COF synthetic strategy endows **UCCOFs** with enhanced PDT effects under NIR irradiation. Surprisingly,

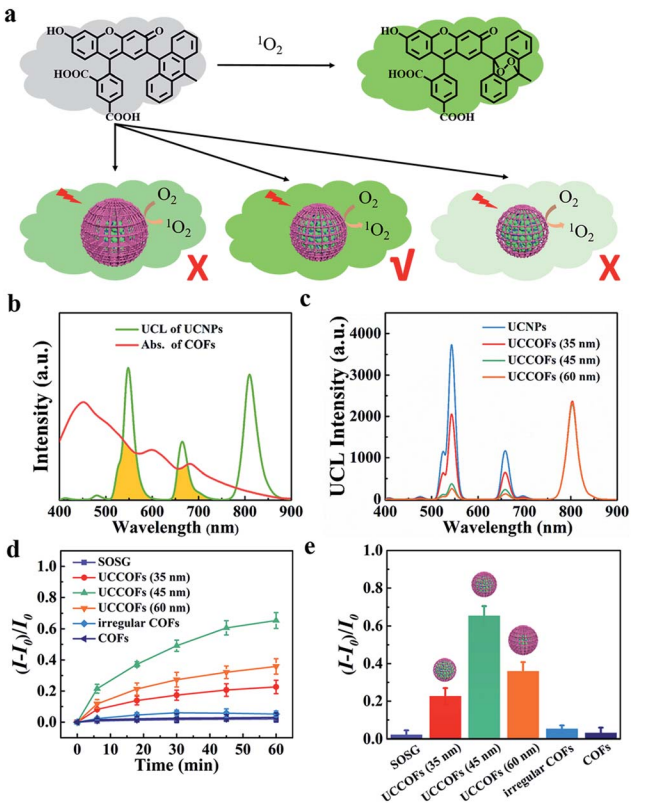

Fig. 2 The photochemical activity of **UCCOFs**. (a) SOSG assay screening of the photochemical activity of **UCCOFs**. (b) The UCL spectrum of UCNPs and the UV-vis absorption (Abs.) spectrum of COFs. (c) The UCL spectra of **UCCOFs** of various sizes. (d) The fluorescence intensity changes of SOSG at 525 nm with increasing irradiation time. (e) The $^1O_2$ generation capacities of **UCCOFs** using different protocols under NIR irradiation by the SOSG assay.

a further increase in size to 60 nm resulted in a decrease in $^1O_2$ production compared with the 45 nm sample (Fig. 2e). We speculate that the increased COF shell thickness would impact the resonance energy transfer efficiency and aggravate stack quenching to restrain the $^1O_2$ generation capacity, resulting in the subdued $^1O_2$ production in the case of 60 nm **UCCOFs** compared to 45 nm **UCCOFs**. Impressively, due to our core-mediated strategy for the controllable synthesis of **UCCOFs**, we could obtain optimized photochemical activity as measured *via* the above-mentioned SOSG assay screening (Fig. 2a). Unless otherwise specified, size-tailored 45 nm **UCCOFs** were employed in the following studies.

The preparation of a self-reporting nanoplatform

Because of the complex physiological environment existing in live organisms, the location and dose of $^1O_2$ from photosensitizers are more difficult to determine *in vivo* than *in vitro*. In order to achieve self-reporting PDT *in vivo*, we constructed an upconverting COF nanoplatform, **UCCOFs-1**, *via* incorporating ICG as the $^1O_2$ reporter (Scheme 1a). As a NIR absorption dye, ICG has been approved by the Food and Drug Administration (FDA) for clinical therapy with high safety levels.[19] Considering the negatively charged and amphipathic nature of ICG, **UCCOFs** were firstly given positive charge through coupling with poly(ethylene imine) (PEI), and then ICG was loaded into the nanopores of **UCCOFs** *via* electrostatic adsorption. After sequential modification, the hydrodynamic diameter gradually increased, as shown by dynamic light scattering (DLS) (Fig. 3a). Compared to **UCCOFs-PEI**, the zeta potential values were reduced after the preparation of **UCCOFs-1** (Fig. 3b), verifying the successful loading of ICG. After sequential modification, **UCCOFs-1** retains the same crystalline structure as **UCCOFs** according to PXRD data (Fig. S7†). The Brunauer–Emmett–Teller (BET) surface area of **UCCOFs-1** showed a sharp reduction compared to that of **UCCOFs** (Fig. S8†), suggesting that the numerous pores and large surface area of the COFs also contribute to the ICG assembly.

ICG showed a broad absorption peak at about 780 nm, overlapping with the UCL of the UCNPs (Fig. 3d). Once oxidized by $^1O_2$, an unstable alkene in the polymethine chain of ICG will break into two parts (Fig. 3c), with a decrease in the absorption peak (Fig. 3e). Because the of spectral overlap between ICG and **UCCOFs**, the UCL of **UCCOFs-1** at 654 nm and 800 nm was quenched compared to **UCCOFs** (Fig. 3f). When exposed to NIR irradiation, **UCCOFs-1** could continue to produce $^1O_2$; therefore, ICG degraded, which resulted in the UCL signal of **UCCOFs-1** being enhanced at 654 nm and 800 nm to visualize $^1O_2$ generation (Fig. 3g). With an increase in the irradiation time, the UCL of **UCCOFs-1** was gradually enhanced (Fig. 3g), indicating the efficient real-time monitoring of $^1O_2$ generation. Compared to free ICG, **UCCOFs-1** had significantly enhanced photostability under 808 nm laser irradiation (Fig. S9†). We suspected that the sheltering effect from the framework architecture of the COFs could effectively improve the photostability of ICG,[26] which possesses poor photostability and often results in failure with respect to practical applications. Furthermore, we also demonstrated that the physiological pH conditions and

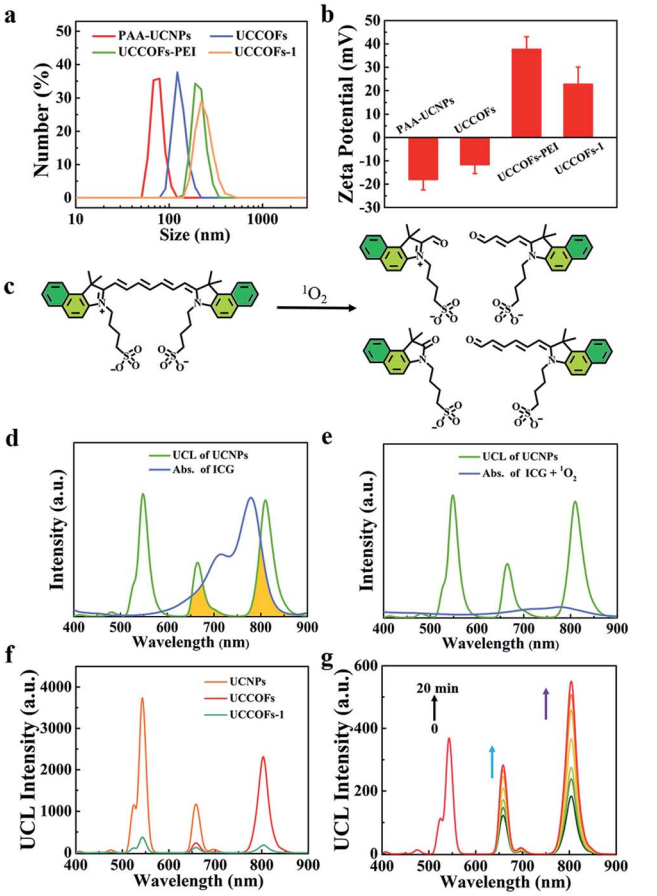

Fig. 3 The preparation of a self-reporting nanoplatform. (a) DLS profiles of **UCCOFs** after sequential post-synthetic modification in aqueous solution. (b) A comparison of the zeta potentials of **UCCOFs** after sequential post-synthetic modification. (c) A schematic illustration of ICG degradation by $^1O_2$. (d) The UCL spectrum of UCNPs and UV-vis absorption (Abs.) spectrum of ICG. (e) The UCL spectrum of UCNPs and UV-vis absorption (Abs.) spectrum of ICG after treatment with $^1O_2$. (f) UCL spectra of UCNPs, **UCCOFs** and **UCCOFs-1**. (g) UCL spectra of **UCCOFs-1** under NIR irradiation at each time period.

acidic tumor microenvironment have no significant effects on ICG breakage under 980 nm laser irradiation (Fig. S10†). The stability of the **UCCOFs-1** assembly was investigated *via* monitoring the UCL intensity. As shown in Fig. S11,† the UCL intensity at 808 nm showed little change under both physiological pH and acidic tumor microenvironment conditions, confirming that there was no ICG leakage under experimental conditions. We also investigated the UCL stability of **UCCOFs-1**. As shown in Fig. S12,† there were no obvious changes in the UCL intensity at 541 nm under 980 nm laser irradiation.

Self-reporting PDT in living cells

The favorable properties of our COF nanoplatform **UCCOFs-1** elucidated above encouraged us to explore its performance for the self-reporting of PDT in live cells. First, we investigated the cellular uptake of **UCCOFs** with HeLa cells. As shown in Fig. 4a and S13,† cells treated with **UCCOFs** exhibited green UCL, indicating the efficient cell internalization of **UCCOFs**.

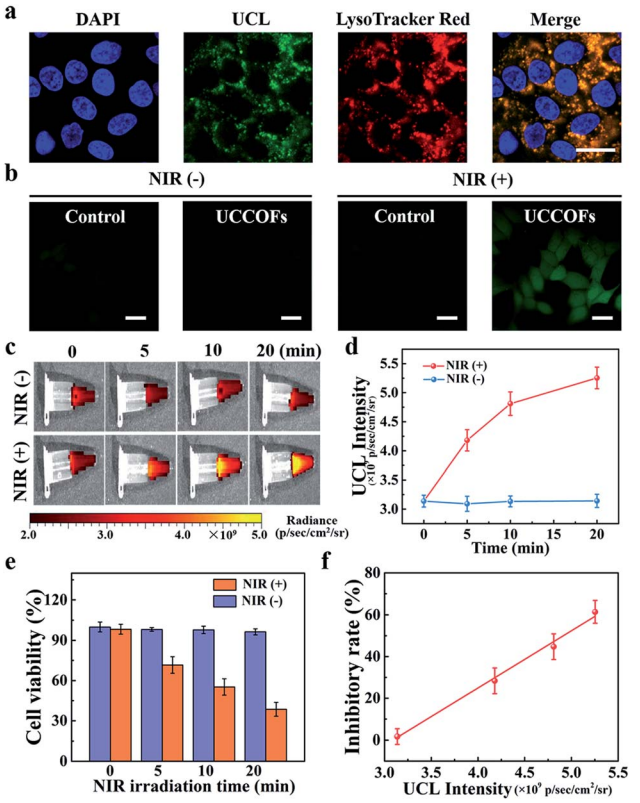

Fig. 4 Self-reporting PDT in living cells. (a) Confocal fluorescence images of HeLa cells treated with **UCCOFs**; scale bar: 20 μm. (b) Intracellular $^1O_2$ production with or without NIR irradiation determined *via* a H_2DCFH-DA assay; scale bar: 20 μm. UCL images (c) and UCL intensity data (d) from HeLa cells after different NIR irradiation times. (e) Cell viability data for HeLa cells with **UCCOFs-1** after different NIR irradiation times. (f) The cell inhibitory rate as a function of UCL intensity for **UCCOFs-1**; $R^2 = 0.994$.

Meanwhile, a colocalization experiment involving **UCCOFs** was operated *via* staining with LysoTracker Red. The red fluorescence from LysoTracker Red and the green UCL from **UCCOFs** overlapped well, suggesting that **UCCOFs** were mainly localized in the lysosomes (Fig. 4a). In order to demonstrate the good biocompatibility of **UCCOFs**, we investigated the cell viability *via* an MTS assay. As shown in Fig. S14,† **UCCOFs** showed negligible cytotoxicity (cell viability > 90%) against both human normal cells (HEK293: human embryonic kidney cells; and LO2: human normal liver cells) and cancer cells (HeLa: human cervical carcinoma cells; and HepG2: human liver cancer cells). Then, $^1O_2$ generation inside cells was examined *via* H_2DCFH-DA (Fig. 4b). HeLa cells treated with **UCCOFs** under 980 nm irradiation showed strong green fluorescence, because the nonfluorescent H_2DCFH-DA was oxidized by $^1O_2$ and produced bright fluorescent DCF (Table S1†), indicating the effective $^1O_2$ generation capacity of **UCCOFs** within live cells. In contrast to the low toxicity in the dark, after NIR irradiation, **UCCOFs-1** showed dose-dependent cytotoxicity, confirming its effectiveness for PDT (Fig. S15†). Furthermore, we also visually evaluated the therapeutic effects through calcein-acetoxymethylester (AM) and propidium iodide (PI) staining and found that increased cell death was only observed after treatment with both **UCCOFs-1** and NIR irradiation (Fig. S16†). The size-tailored enhanced PDT efficiency towards HeLa cells can also be observed in Fig. S17.† **UCCOFs** (45 nm) exhibited better therapeutic effects than both 60 nm **UCCOFs** and 35 nm **UCCOFs**, which is in good agreement with the above SOSG assay results.

Next, we investigated the cell cytotoxicity of **UCCOFs-1** over different irradiation time periods. At the end of different irradiation time periods, we immediately checked the UCL of HeLa cells. As shown in Fig. 4c and d, with prolonged irradiation time, the UCL intensity gradually enhanced. Over the same length of time without NIR irradiation, the UCL intensity of the control group remained unchanged. After another 24 h of incubation, the cell viabilities gradually reduced as the irradiation time increased (Fig. 4e). Also, the cell viabilities of the control group without NIR irradiation show no significant changes. Excitingly, there is a good linear relationship between cell inhibition and UCL intensity (Fig. 4f). This means that we are able to predict cellular viability *via* the real-time monitoring of the UCL intensity of **UCCOFs-1** without needing to wait for more than one day to test the cellular survival. Moreover, inadequate treatment could be reconsidered in a timely fashion, while overtreatment could be suspended immediately.

Self-reporting of PDT *in vivo*

Inherent issues will impact on the future of conventional PDT for further clinical applications, such as the use of visible light excitation, excess photosensitizers, and high-power laser radiation, the existence of delayed therapeutic feedback, and so on (Fig. 5a). Although NIR-excited PDT has been reported,[44,46] the real-time monitoring and prediction of treatment progress is still difficult to realize *in vivo*. The good performance of **UCCOFs-1** motivated us to further evaluate its *in vivo* self-reporting antitumor activity. Mice bearing 4T1 breast tumors were intratumorally injected with **UCCOFs-1** and they then received NIR irradiation for different time periods (Scheme S2†). Meanwhile, the UCL of **UCCOFs-1** in the tumor region was monitored after different irradiation times (Scheme S2†). We found that as the irradiation time increased, the UCL intensity gradually increased (Fig. 5b and S18†). Also, the UCL intensity of the control group without NIR irradiation showed no significant changes, also suggesting that **UCCOFs-1** could remain stable during the experimental process. Furthermore, the tumor sizes were continuously monitored for two weeks after NIR irradiation. As shown in Fig. 5c and S19,† the tumors treated with **UCCOFs-1** + NIR laser irradiation showed efficient suppression compared with those treated with only **UCCOFs-1**, NIR laser irradiation, or saline. Importantly, for those tumors treated with **UCCOFs-1** + NIR, as the NIR irradiation time increased, the tumor size gradually diminished. Analysis of hematoxylin and eosin (H&E) stained tumor sections further confirmed the gradual enhancement of PDT efficacy as the irradiation time increased (Fig. 5e). In addition, there were no significant changes in mouse body weight during the experimental period (Fig. S20†) and no obvious pathologic changes in the primary organs (Fig. S21†), which suggested the biosafety of this method. Notably, there was a good linear relationship

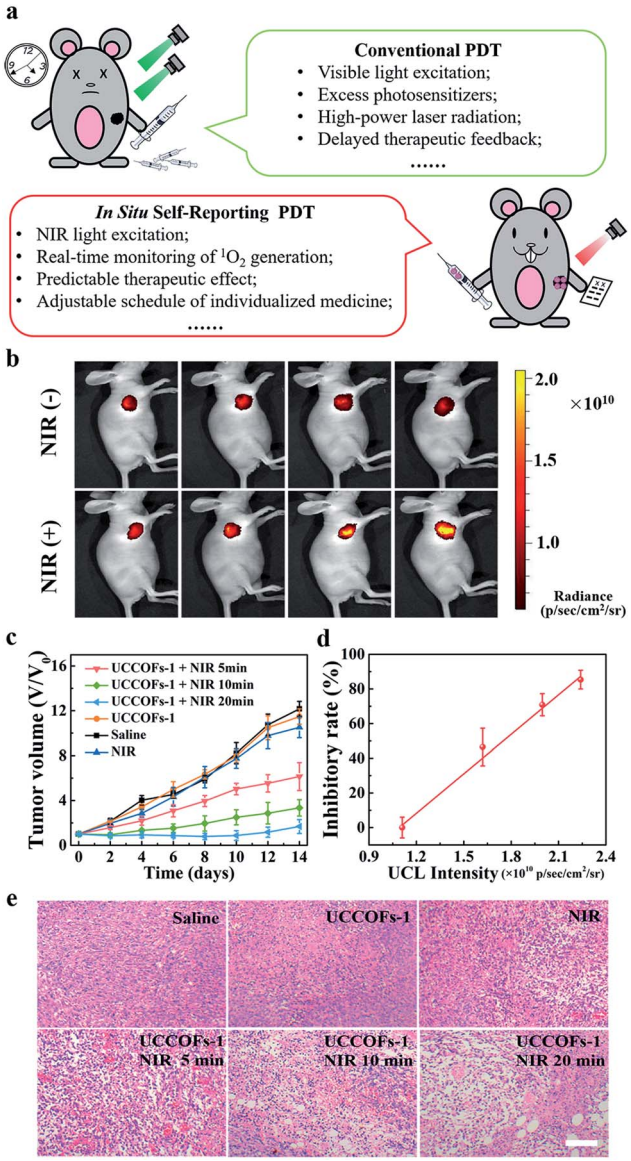

Fig. 5 Self-reporting PDT *in vivo*. (a) A comparison between conventional PDT and our *in situ* self-reporting PDT. (b) The UCL intensity of 4T1 tumor-bearing live mice after the intratumor injection of **UCCOFs-1** at different NIR irradiation times. (c) The tumor growth curves after different treatments with or without 980 nm irradiation (1.2 W cm^{-2}). (d) The tumor inhibitory rate as a function of UCL intensity for **UCCOFs-1**; $R^2 = 0.997$. (e) H&E stained images of tumor sections after different treatments; scale bar: 50 μm.

between the tumor inhibitory rate and the UCL signal intensity in the tumor region (Fig. 5d), indicating the feasibility of the *in situ* self-reporting PDT strategy *in vivo*. Thus, the *in situ* self-reporting PDT strategy may effectively avoid delayed treatment observations and allow timely adjustments to be made to therapeutic schedules (Fig. 5a).

Conclusions

In summary, we developed NIR-excited COF hybrid nanoparticles, **UCCOFs**, *via* core-mediated imine polymerization. And by virtue of the size-tailored strategy, **UCCOFs** acquired highly efficient PDT capabilities. To achieve therapeutic process monitoring, we adequately took advantage of COFs with enormous porosity and established an upconverting COF nanoplatform through the incorporation of ICG. Our nanoplatform performed well in self-reporting the direct location and dose of $^1O_2$ *via* NIR activated UCL during *in vivo* PDT for cancer. Through analyzing the relationship between the luminescence intensity and tumor inhibition rates, such an upconverting COF nanoplatform may be able to predict the therapeutic effects in a timely fashion and thereby allow an adjustable schedule for individualized medicine, which is promising for avoiding overtreatment and reducing side effects.

Ethical statement

All animal operations were carried out in compliance with the relevant laws and approved by the Institutional Animal Care and Use Committee of Hunan University (Changsha, China).

Conflicts of interest

There are no conflicts to declare.

Acknowledgements

This work was supported by the National Natural Science Foundation of China (Grants 21705037, 21974039, 21675043, 21890744, 51872088, 21804039), and the Hunan Provincial Natural Science Foundation of China (2018JJ3092).

Notes and references

1 B. Yang, Y. Chen and J. Shi, *Chem. Rev.*, 2019, **119**, 4881–4985.
2 S. Kwon, H. Ko, D. G. You, K. Kataoka and J. H. Park, *Acc. Chem. Res.*, 2019, **52**, 1771–1782.
3 Z. Zhou, J. Song, L. Nie and X. Chen, *Chem. Soc. Rev.*, 2016, **45**, 6597–6626.
4 W. Fan, P. Huang and X. Chen, *Chem. Soc. Rev.*, 2016, **45**, 6488–6519.
5 L. Cheng, X. Wang, F. Gong, T. Liu and Z. Liu, *Adv. Mater.*, 2019, 1902333.
6 X. Qian, Y. Zheng and Y. Chen, *Adv. Mater.*, 2016, **28**, 8097–8129.
7 P. Huang, X. Qian, Y. Chen, L. Yu, H. Lin, L. Wang, Y. Zhu and J. Shi, *J. Am. Chem. Soc.*, 2017, **139**, 1275–1284.
8 G. Song, L. Cheng, Y. Chao, K. Yang and Z. Liu, *Adv. Mater.*, 2017, **29**, 1700996.
9 J. Liu, Y. Yang, W. Zhu, X. Yi, Z. Dong, X. Xu, M. Chen, K. Yang, G. Lu, L. Jiang and Z. Liu, *Biomaterials*, 2016, **97**, 1–9.
10 N. Lu, W. Fan, X. Yi, S. Wang, Z. Wang, R. Tian, O. Jacobson, Y. Liu, B. C. Yung, G. Zhang, Z. Teng, K. Yang, M. Zhang, G. Niu, G. Lu and X. Chen, *ACS Nano*, 2018, **12**, 1580–1591.

11 B. Ma, S. Wang, F. Liu, S. Zhang, J. Duan, Z. Li, Y. Kong, Y. Sang, H. Liu, W. Bu and L. Li, *J. Am. Chem. Soc.*, 2019, **141**, 849–857.
12 L. S. Lin, T. Huang, J. Song, X. Y. Ou, Z. Wang, H. Deng, R. Tian, Y. Liu, J. F. Wang, Y. Liu, G. Yu, Z. Zhou, S. Wang, G. Niu, H. H. Yang and X. Chen, *J. Am. Chem. Soc.*, 2019, **141**, 9937–9945.
13 J. P. Celli, B. Q. Spring, I. Rizvi, C. L. Evans, K. S. Samkoe, S. Verma, B. W. Pogue and T. Hasan, *Chem. Rev.*, 2010, **110**, 2795–2838.
14 D. O. Lapotko and V. P. Zharov, *Lasers Surg. Med.*, 2005, **36**, 22–30.
15 B. R. Sharma, *Infect. Dis. Clin. N. Am.*, 2007, **21**, 745–759.
16 T. Zhang, Y. Li, Z. Zheng, R. Ye, Y. Zhang, R. T. K. Kwok, J. W. Y. Lam and B. Z. Tang, *J. Am. Chem. Soc.*, 2019, **141**, 5612–5616.
17 F. Zou, W. Zhou, W. Guan, C. Lu and B. Z. Tang, *Anal. Chem.*, 2016, **88**, 9707–9713.
18 L. Zhang, J. Lei, F. Ma, P. Ling, J. Liu and H. Ju, *Chem. Commun.*, 2015, **51**, 10831–10834.
19 C. Y. Tang, F. Y. Wu, M. K. Yang, Y. M. Guo, G. H. Lu and Y. H. Yang, *Int. J. Mol. Sci.*, 2016, **17**, 219.
20 Q. Pei, X. Hu, X. Zheng, S. Liu, Y. Li, X. Jing and Z. Xie, *ACS Nano*, 2018, **12**, 1630–1641.
21 R. Ruiz-Gonzalez, R. Bresoli-Obach, O. Gulias, M. Agut, H. Savoie, R. W. Boyle, S. Nonell and F. Giuntini, *Angew. Chem., Int. Ed.*, 2017, **56**, 2885–2888.
22 Z. Zhou, J. Song, R. Tian, Z. Yang, G. Yu, L. Lin, G. Zhang, W. Fan, F. Zhang, G. Niu, L. Nie and X. Chen, *Angew. Chem., Int. Ed.*, 2017, **56**, 6492–6496.
23 X. Li, D. Lee, J. D. Huang and J. Yoon, *Angew. Chem., Int. Ed.*, 2018, **57**, 9885–9890.
24 L. Jiao, X. Zhang, J. Cui, X. Peng and F. Song, *ACS Appl. Mater. Interfaces*, 2019, **11**, 25750–25757.
25 Y. Gao, X. Wang, X. He, Z. He, X. Yang, S. Tian, F. Meng, D. Ding, L. Luo and B. Z. Tang, *Adv. Funct. Mater.*, 2019, **29**, 1902673.
26 P. Wang, F. Zhou, C. Zhang, S. Y. Yin, L. Teng, L. Chen, X. X. Hu, H. W. Liu, X. Yin and X. B. Zhang, *Chem. Sci.*, 2018, **9**, 8402–8408.
27 G. Zhang, X. Li, Q. Liao, Y. Liu, K. Xi, W. Huang and X. Jia, *Nat. Commun.*, 2018, **9**, 2785.
28 V. S. Vyas, M. Vishwakarma, I. Moudrakovski, F. Haase, G. Savasci, C. Ochsenfeld, J. P. Spatz and B. V. Lotsch, *Adv. Mater.*, 2016, **28**, 8749–8754.
29 S. Mitra, H. S. Sasmal, T. Kundu, S. Kandambeth, K. Illath, D. Diaz Diaz and R. Banerjee, *J. Am. Chem. Soc.*, 2017, **139**, 4513–4520.
30 G. Das, F. Benyettou, S. K. Sharama, T. Prakasam, F. Gandara, V. A. de la Pena-O'Shea, N. Saleh, R. Pasricha, R. Jagannathan, M. A. Olson and A. Trabolsi, *Chem. Sci.*, 2018, **9**, 8382–8387.
31 Q. Guan, D. D. Fu, Y. A. Li, X. M. Kong, Z. Y. Wei, W. Y. Li, S. J. Zhang and Y. B. Dong, *iScience*, 2019, **14**, 180–198.
32 L. Zhang, S. Wang, Y. Zhou, C. Wang, X.-Z. Zhang and H. Deng, *Angew. Chem., Int. Ed.*, 2019, **58**, 14213–14218.
33 R. Freund, U. Lachelt, T. Gruber, B. Ruhle and S. Wuttke, *ACS Nano*, 2018, **12**, 2094–2105.
34 G. Lin, H. Ding, R. Chen, Z. Peng, B. Wang and C. Wang, *J. Am. Chem. Soc.*, 2017, **139**, 8705–8709.
35 N. Keller, M. Calik, D. Sharapa, H. R. Soni, P. M. Zehetmaier, S. Rager, F. Auras, A. C. Jakowetz, A. Gorling, T. Clark and T. Bein, *J. Am. Chem. Soc.*, 2018, **140**, 16544–16552.
36 X. Chen, M. Addicoat, E. Jin, L. Zhai, H. Xu, N. Huang, Z. Guo, L. Liu, S. Irle and D. Jiang, *J. Am. Chem. Soc.*, 2015, **137**, 3241–3247.
37 X. Zheng, L. Wang, Q. Pei, S. He, S. Liu and Z. Xie, *Chem. Mater.*, 2017, **29**, 2374–2381.
38 J. Hynek, J. Zelenka, J. Rathousky, P. Kubat, T. Ruml, J. Demel and K. Lang, *ACS Appl. Mater. Interfaces*, 2018, **10**, 8527–8535.
39 R. Chen, J. L. Shi, Y. Ma, G. Lin, X. Lang and C. Wang, *Angew. Chem., Int. Ed.*, 2019, **58**, 6430–6434.
40 Y. Zhang, L. Zhang, Z. Wang, F. Wang, L. Kang, F. Cao, K. Dong, J. Ren and X. Qu, *Biomaterials*, 2019, **223**, 119462.
41 D. Wang, Z. Zhang, L. Lin, F. Liu, Y. Wang, Z. Guo, Y. Li, H. Tian and X. Chen, *Biomaterials*, 2019, **223**, 119459.
42 M. Xu, X. Zou, Q. Su, W. Yuan, C. Cao, Q. Wang, X. Zhu, W. Feng and F. Li, *Nat. Commun.*, 2018, **9**, 2698.
43 J. Peng, A. Samanta, X. Zeng, S. Han, L. Wang, D. Su, D. T. Loong, N. Y. Kang, S. J. Park, A. H. All, W. Jiang, L. Yuan, X. Liu and Y. T. Chang, *Angew. Chem., Int. Ed.*, 2017, **56**, 4165–4169.
44 Z. Yu, W. Pan, N. Li and B. Tang, *Chem. Sci.*, 2016, **7**, 4237–4244.
45 Z. Yang, K. Y. Loh, Y. T. Chu, R. Feng, N. S. R. Satyavolu, M. Xiong, S. M. Nakamata Huynh, K. Hwang, L. Li, H. Xing, X. Zhang, Y. R. Chemla, M. Gruebele and Y. Lu, *J. Am. Chem. Soc.*, 2018, **140**, 17656–17665.
46 Y. Li, Z. Di, J. Gao, P. Cheng, C. Di, G. Zhang, B. Liu, X. Shi, L. D. Sun, L. Li and C. H. Yan, *J. Am. Chem. Soc.*, 2017, **139**, 13804–13810.
47 T. Liang, Z. Li, P. Wang, F. Zhao, J. Liu and Z. Liu, *J. Am. Chem. Soc.*, 2018, **140**, 14696–14703.
48 J. Zhao, J. Gao, W. Xue, Z. Di, H. Xing, Y. Lu and L. Li, *J. Am. Chem. Soc.*, 2018, **140**, 578–581.
49 X. Zeng, S. Chen, A. Weitemier, S. Han, A. Blasiak, A. Prasad, K. Zheng, Z. Yi, B. Luo, I.-H. Yang, N. Thakor, C. Chai, K.-L. Lim, T. J. McHugh, A. H. All and X. Liu, *Angew. Chem., Int. Ed.*, 2019, **58**, 9262–9268.
50 X. Qin, J. Xu, Y. Wu and X. Liu, *ACS Cent. Sci.*, 2019, **5**, 29–42.
51 Z. Hou, K. Deng, M. Wang, Y. Liu, M. Chang, S. Huang, C. Li, Y. Wei, Z. Cheng, G. Han, A. A. Al Kheraif and J. Lin, *Chem. Mater.*, 2019, **31**, 774–784.
52 B. Liu, C. Li, P. Yang, Z. Hou and J. Lin, *Adv. Mater.*, 2017, **29**, 1605434.
53 D. Yang, P. Ma, Z. Hou, Z. Cheng, C. Li and J. Lin, *Chem. Soc. Rev.*, 2015, **44**, 1416–1448.
54 S. Kandambeth, D. B. Shinde, M. K. Panda, B. Lukose, T. Heine and R. Banerjee, *Angew. Chem., Int. Ed.*, 2013, **52**, 13052–13056.
55 N. Huang, X. Chen, R. Krishna and D. Jiang, *Angew. Chem., Int. Ed.*, 2015, **54**, 2986–2990.

56 T. Ma, E. A. Kapustin, S. X. Yin, L. Liang, Z. Zhou, J. Niu, L.-H. Li, Y. Wang, J. Su, J. Li, X. Wang, W. D. Wang, W. Wang, J. Sun and O. M. Yaghi, *Science*, 2018, **361**, 48–52.
57 H. Ding, J. Li, G. Xie, G. Lin, R. Chen, Z. Peng, C. Yang, B. Wang, J. Sun and C. Wang, *Nat. Commun.*, 2018, **9**, 5234.
58 P. F. Wei, M. Z. Qi, Z. P. Wang, S. Y. Ding, W. Yu, Q. Liu, L. K. Wang, H. Z. Wang, W. K. An and W. Wang, *J. Am. Chem. Soc.*, 2018, **140**, 4623–4631.
59 S. Wang, Q. Wang, P. Shao, Y. Han, X. Gao, L. Ma, S. Yuan, X. Ma, J. Zhou, X. Feng and B. Wang, *J. Am. Chem. Soc.*, 2017, **139**, 4258–4261.
60 S. Y. Ding, M. Dong, Y. W. Wang, Y. T. Chen, H. Z. Wang, C. Y. Su and W. Wang, *J. Am. Chem. Soc.*, 2016, **138**, 3031–3037.
61 J. Tan, S. Namuangruk, W. Kong, N. Kungwan, J. Guo and C. Wang, *Angew. Chem., Int. Ed.*, 2016, **55**, 13979–13984.
62 N. Huang, P. Wang and D. Jiang, *Nat. Rev. Mater.*, 2016, **1**, 16068.